Published in final edited form as:
Neuroimage. 2011 March 15; 55(2): 597–606. doi:10.1016/j.neuroimage.2010.11.084.

Physiological noise and signal-to-noise ratio in fMRI with multi-channel array coils

Christina Triantafyllou[1,2], **Jonathan R. Polimeni**[2], and **Lawrence L. Wald**[2,3]

[1]Athinoula A. Martinos Imaging Center at McGovern Institute for Brain Research, Massachusetts Institute of Technology, Cambridge, MA, USA

[2]Athinoula A. Martinos Center for Biomedical Imaging, Massachusetts General Hospital, Dept. of Radiology, Harvard Medical School, Charlestown, MA, USA

[3]Harvard-Massachusetts Institute of Technology (MIT) Division of Health Sciences and Technology, Cambridge, Massachusetts, USA

Abstract

Sensitivity in BOLD fMRI is characterized by the Signal to Noise Ratio (SNR) of the time-series (tSNR), which contains fluctuations from thermal and physiological noise sources. Alteration of an acquisition parameter can affect the tSNR differently depending on the relative magnitude of the physiological and thermal noise, therefore knowledge of this ratio is essential for optimizing fMRI acquisitions. In this study, we compare image and time-series SNR from array coils at 3T with and without parallel imaging (GRAPPA) as a function of image resolution and acceleration. We use the "absolute unit" SNR method of Kellman and McVeigh to calculate the image SNR (SNR_0) in a way that renders it comparable to tSNR, allowing determination of the thermal to physiological noise ratio, and the pseudo-multiple replica method to quantify the image noise alterations due to the GRAPPA reconstruction. The Kruger and Glover noise model, in which the physiological noise standard deviation is proportional to signal strength, was found to hold for the accelerated and non-accelerated array coil data. Thermal noise dominated the EPI time-series for medium to large voxel sizes for single-channel and 12-channel head coil configurations, but physiological noise dominated the 32-channel array acquisition even at 1mm × 1mm × 3mm resolution. At higher acceleration factors, image SNR is reduced and the time-series becomes increasingly thermal noise dominant. However, the tSNR reduction is smaller than the reduction in image SNR due to the presence of physiological noise.

Keywords

physiological noise; parallel imaging; array coils; fMRI; GRAPPA; SNR; 32-channel coil; resolution

Correspondence should be directed to: Christina Triantafyllou, Ph.D., A.A Martinos Imaging Center at McGovern Institute for Brain Research, Massachusetts Institute of Technology, 77 Massachusetts Avenue, Bldg 46, Room 46-1165, Cambridge, MA 02139, USA. Tel: +1 617 324 2706, Fax:+1 617 324 2701, ctrianta@mit.edu.

INTRODUCTION

Our ability to detect small changes in image intensity associated with subtle brain activation in the fMRI experiment (e.g. the BOLD effect) is determined by the field strength, echo time and time-series SNR of the experiment (where time-series SNR is defined as mean intensity of an ROI or pixel in the time-series divided by its standard deviation across time). Because the first two of these parameters are easily controlled, time-series SNR is the most important metric for sensitivity in a given fMRI acquisition protocol. The total variance (noise) in time-series, however, is comprised of both thermal image noise and physiological fluctuations which modulate the image intensity over time. Previous studies of the physiological noise in fMRI time-series have shown that the standard deviation of the physiological noise is proportional to the signal strength. Changes in the MR acquisition protocol that alter the MR signal level, therefore, also alter the size of the physiological noise contribution (Kruger and Glover 2001), (Triantafyllou et al. 2005). As the signal increases (e.g., from higher field strengths, the use of array coils, or changes in voxel volume), the physiological noise increases proportionally. This is problematic since improving detection sensitivity, for example with array coils, will not translate to improved tSNR for fMRI if the time-series variance is dominated by physiological noise. In this case, it is important to translate the improved detection sensitivity toward other desirable directions, such as increased spatial resolution or additional parallel imaging acceleration (with reduced susceptibility-induced image distortion).

With a few exceptions (de Zwart et al. 2002, Triantafyllou et al. 2008), most studies of physiological noise to date have not analyzed array coil acquisitions, likely because they either predated the widespread use of array coils in fMRI or because of the difficulty of computing the image SNR (SNR_0) of the array coil image in a way that renders it comparable to the tSNR, so that the relative contributions of thermal and physiological noise can be determined accurately. In our previous studies, we characterized the time-series noise as a function of field strength, image resolutions, echo times and other EPI acquisition parameters (Triantafyllou et al. 2005) as well as the effect of smoothing on tSNR (Triantafyllou et al. 2006). However, these studies utilized single-channel volume coils with considerably lower sensitivity than the multi-channel coils currently in use. Present fMRI protocols mostly utilize array coils of at least 8 channels, often combined with parallel imaging methods such as SENSE (Pruessmann et al. 1999) or GRAPPA (Griswold et al. 2002) to accelerate the EPI acquisitions in order to reduce susceptibility distortions. These acceleration methods have been shown to differentially affect the physiological and thermal components of the total time-series variance by principally enhancing the thermal noise component (de Zwart et al. 2002). In our study, we utilize the absolute SNR units (Kellman and McVeigh 2005) and GRAPPA g-factor analysis (Robson et al. 2008) to determine the tradeoffs thermal and physiological noise for standard acquisition protocols at 3T, using a commercial single-channel, 12-channel (12Ch) and 32-channel (32Ch) head coils. We therefore re-examine the tradeoffs between imaging parameters such as resolution and acceleration have on tSNR and assess the resulting balance between thermal and physiological noise.

Accurately assessing the SNR of an image acquired with an array coil in a manner that can be directly compared to time-series SNR measurements requires a number of considerations. Kellman and McVeigh (Kellman and McVeigh 2005) elegantly described the series of correction factors needed to produce SNR in “absolute units”, which are exactly what is needed for comparing image (thermal) SNR (SNR_0) to time-series SNR (tSNR) when arrays are used. The tSNR is expected to equal the SNR_0 in a phantom measurement on a stable scanner only when all of these correction factors are taken into account. For example, the internal filtering bandwidth of the receivers must be measured and accounted for.

Additionally a generalization of the standard Rician correction factor (used to characterize the noise as Gaussian for single channel coils, (Gudbjartsson and Patz 1995) must be applied to array coil SNR measurements to account for the statistical distribution present in the magnitude images typically analyzed for fMRI (Constantinides et al. 1997). Although often considered unimportant for images with SNR above 10, a closer look shows that the correction factor for the statistical distribution is dependent on the number of array coil elements and can be significant for highly parallel arrays (e.g. 32Ch arrays). For example, the noise statistic bias correction lowers the measured SNR by a factor of 0.6 for a 32Ch in an image with SNR = 13. This bias correction factor is particularly important for array coil physiological noise characterization, since it is not a simple scale factor; it depends non-linearly on both SNR itself and the number of array elements. Finally, the use of parallel image reconstructions further complicates analysis of the tradeoffs between image and time-series SNR. While simple methods exist for calculating the noise enhancement of the thermal image noise in SENSE (the SENSE g-factor) (Pruessmann et al. 1999), for GRAPPA, the other commonly employed parallel reconstruction method, the equivalent of the g-factor calculation has only been recently addressed (Robson et al. 2008, Breuer et al. 2009).

De Zwart and colleagues have examined the physiological to thermal noise trade-off for an acceleration factor of 2 (R=2) SENSE method and a 1.5T four-element array at a single resolution (3.4mm × 3.4mm × 4mm). Their data supports the theory that the SENSE g-factor and $\sqrt{R}$ penalty alters only SNR_0 and not the physiological noise component. Therefore, for acquisitions dominated by physiological noise, the image degradation associated with SENSE does not meaningfully degrade the tSNR (de Zwart et al. 2002). Since the penalty to tSNR from the noise amplification and acceleration factor depends on the relative contribution of physiological and image noise, we seek to extend this type of study to multiple resolutions and acceleration factors as well as increased field strength (3T) and more highly parallel array coils (12Ch and 32Ch). We also utilize the absolute SNR units of Kellman and McVeigh, which allow us to directly compare image and time-series SNR and their associated variances instead of being restricted to analyzing the ratio of the accelerated image or time-series variance to the non-accelerated image or variance. Finally, we extend the study to accelerated fMRI acquisitions reconstructed with the GRAPPA method.

THEORY

Physiological Fluctuations

Previous studies (Kruger and Glover 2001, Triantafyllou et al. 2005) have examined the relationship between the fMRI tSNR and the SNR_0 using a model where physiological noise standard deviation is proportional to signal. The total noise, σ_t, in the fMRI time-series is modeled as the sum of the Gaussian thermal image noise and the physiological signal fluctuations (cardiac, respiratory and hemodynamic induced signal modulations), and these two noise sources are presumed to be statistically independent: $\sigma_t = \sqrt{\sigma_0^2 + \sigma_p^2}$, where σ_0 is the thermal image noise and σ_p is the physiological noise standard deviation. Here, we assume that system instabilities are relatively small. Because physiological noise is modeled as scaling with the amplitude of the MR signal (S) with proportionality constant λ, or $\sigma_p = \lambda S$, the model predicts that

$$tSNR = \frac{SNR_0}{\sqrt{1+\lambda^2 \cdot SNR_0{}^2}} \quad (1)$$

For large SNR_0, tSNR is asymptotically limited to $1/\lambda$. This result shows that increasing SNR_0 through increasing the field strength or altering the coil design can produce limited improvements in tSNR if SNR_0 is already high.

The ratio of physiological noise to thermal noise can be estimated from measurements of tSNR and SNR_0 using the equation

$$\frac{\sigma_p}{\sigma_0} = \sqrt{\left(\frac{SNR_0}{tSNR}\right)^2 - 1} \tag{2}$$

When the above ratio is less than 1, the fMRI time-series is thermal image noise dominated, and when the ratio is greater than 1, physiological fluctuations are dominant. When $\sigma_p/\sigma_0 \gg 1$, tSNR is near its asymptotic limit and will not significantly increase if the image sensitivity is increased, for example by improved array coil design. Similarly, the noise enhancement from the SENSE or GRAPPA "g-factor" (coil geometry factor) and the noise penalty associated with the reduced acquisition time given by the acceleration factor *R*, are not expected to translate to large losses of tSNR for physiological noise dominated measurements if tSNR is already near its asymptotic limit, since these noise amplification effects impact SNR_0 only. The goal of this work is to verify this theory for array coil acquisitions and characterize the physiological to thermal noise ratio for common acquisition protocols (employing array coils and parallel imaging acceleration).

Image SNR using Phased Arrays

A conventional method for estimating SNR_0 in an array coil image is to measure the uniformly sampled noise data from each channel (in the absence of RF excitation) and compute the channel noise covariance matrix, $\boldsymbol{\psi}$, which describes the thermal noise variance in each channel and the covariance between pairs of channels. Here we deviate slightly from conventional terminology (Roemer et al. 1990, Kellman and McVeigh 2005) by distinguishing between the root sum-of-squares (rSoS) combination—where the noise covariance is not included in the coil combination weighting—and the noise covariance weighted root sum-of-squares (cov-rSoS) combination. For these two methods, the final image pixel intensity, $\boldsymbol{I}$, is combined from the signal vector $\boldsymbol{S}$ (a vector of image intensities at this pixel location across all coils), and is given by

$$I^{rS_0S} = \sqrt{S^H S} \tag{3}$$

$$SNR^{cov-rS_0S} = \sqrt{S^H \Psi^{-1} S} \tag{4}$$

where $\boldsymbol{S}^H$ denotes the Hermitian transpose of $\boldsymbol{S}$ and $\boldsymbol{\psi}^{-1}$ is the inverse of the noise covariance matrix $\boldsymbol{\psi}$. Here the channel combination is normalized using the uniform noise normalization (Roemer et al. 1990), (Wright and Wald 1997).

The image SNR for the root-sum-of-squares (rSoS) combination (Roemer et al. 1990) can be expressed as

$$SNR^{rS_0S} = \frac{S^H S}{\sqrt{S^H \Psi S}} \tag{5}$$

While the image SNR for the noise covariance weighted root-sum-of-squares reconstruction (cov-rSoS) (Roemer et al. 1990, Wright and Wald 1997) is

$$SNR^{cov-rS_0S} = \sqrt{S^H \Psi^{-1} S} \tag{6}$$

For both combination methods, an implicit normalization forces the noise to be uniform across the image (Roemer et al. 1990).

While the above SNR equations are useful, they do not make the detailed corrections needed to render the array SNR_0 comparable to tSNR such that a phantom measurement on a stable system would produce identical SNR maps for the image and for the time-series (SNR_0 = tSNR). The steps needed to make these two measurements comparable were described by Kellman and McVeigh (Kellman and McVeigh 2005). This method utilizes uniformly sampled noise data from each channel (in the absence of RF excitation) and computes SNR_0 for the image accounting for how each step in the image reconstruction affects the statistics of the thermal noise present in the final image. The method employs four correction factors beyond what is described by Eq. 5 and 6. Firstly, the assumption that the thermal noise is white is re-examined. The noise spectrum in an MR image is determined by the various analog and digital filters applied to the received signal and because there is a shape to these filters, the spectrum of the noise is not a perfect "top-hat" function; therefore, the samples are not fully temporally uncorrelated. Per Kellman et al., (Kellman and McVeigh 2005) a "noise equivalent bandwidth" is defined as the bandwidth of the ideal top-hat filter which, when fed with white noise, produces the same noise power at the output as that found in the measurement. This noise equivalent bandwidth correction factor is measured by sampling noise-only data and determining the ratio of the mean-squared power of the noise spectrum to its value at the center of the spectrum. For typical scanners, the correction factor for a non-white spectrum scales the noise level by a factor $\boldsymbol{b}_{\mathbf{noise}} \approx 0.8$, and the noise bandwidth correction factor is straightforward to estimate from the same noise scan used to estimate the noise covariance. Then the estimated noise covariance matrix $\boldsymbol{\psi}$ is scaled by dividing by this factor.

The second scaling factor accounts for the noise averaging performed during the Fourier transform, by normalizing the noise covariance matrix by the number of samples contributing to each image pixel, $\boldsymbol{N}_{\mathbf{acq}}$. Note that this scaling is based on the total number of acquired *k*-space samples for a given image acquisition, including oversampling, not the final number of image pixels which can differ, e.g., for partial Fourier acquisitions.

The noise covariance matrix must be normalized by the third correction factor of $\sqrt{2}$ since the observation model assumes that the signal is real-valued while the noise is complex-valued with independent and identically distributed real and imaginary parts (i.e., drawn from a zero-mean Gaussian distribution with equal variances) (Kellman and McVeigh 2007).

A fourth correction factor, $\boldsymbol{k}$, also needs to be applied, to account for the incorrect assumption of Gaussian-distributed noise statistics in magnitude images (Henkelman 1985, Constantinides et al. 1997, Kellman and McVeigh 2005). This correction is the generalization of the well-known Rician distribution correction (Gudbjartsson and Patz 1995) to multiple-channel coil arrays. The noise statistics for the final magnitude image from an array follow a non-central chi distribution and a correction for this bias has been calculated (Constantinides et al. 1997).

Because this bias is itself a function of pixel intensity it varies over the image and the correction factor is not a simple scaling of the SNR map, thus it must be calculated and applied on a pixel-by-pixel basis. While this correction is most important for low-SNR data, the SNR bias becomes more substantial and can be significant even for images with moderate-to-high SNR for arrays consisting of large numbers of elements. Therefore, this normalization is crucial to the accurate comparison between SNR_0 and tSNR for data collected with array coils and for comparisons of these SNR metrics between different sized arrays. Since this correction factor is not an image intensity correction—it is a correction of the SNR map to account for the changes in noise statistic distributions—it is only applied to the SNR maps and not the images themselves and must be applied to both the SNR_0 and tSNR maps prior to their comparison using Eq. 1 or 2.

Since the plots provided by Constantinides et al. (Constantinides et al. 1997) only extend to 4 array elements, and Kellman and McVeigh (Kellman and McVeigh 2005) included up to 32 array elements, we regenerated their graphs to include up to 128 elements. Fig. 1 shows the magnitude correction factors as a function of the measured SNR (either SNR_0 or tSNR) for different array sizes. Here, the measured SNR refers to the SNR value which would be obtained from the magnitude images assuming a Gaussian distribution for the image noise. While the bias correction factors converge to unity for high SNR, there are significant deviations from unity for larger arrays for SNRs in the range of 10 to 50. For example, a pixel with an SNR of 20 acquired with a 32Ch coil must be scaled by a factor of 0.869, compared with 0.953 for a 12Ch coil and 0.998 with a single-channel coil.

Parallel imaging (SENSE or GRAPPA) introduces spatially-variant noise amplification in the reconstructed images, leading to image SNR degradation associated with the acceleration factor (R) and the coil geometry factor (g-factor). The noise is increased compared to the non-accelerated image by a factor of $g\sqrt{R}$. In the current study we accelerate images using the GRAPPA (Griswold et al. 2002) parallel imaging method. The GRAPPA image SNR was calculated using the method described by Robson et al. (Robson et al. 2008). This method calculates the image SNR in a GRAPPA reconstruction through a Monte Carlo simulation in which synthetic thermal noise is generated with statistics that match the noise covariance matrix, and this noise is added to the measured *k*-space data prior to image reconstruction. The image reconstruction, including the application of the GRAPPA kernel to estimate missing lines in *k*-space and the final channel combination step, propagates this synthetic noise through to the resulting magnitude image. This process is then repeated for many trials to generate an ensemble of synthetic images. The SNR_0 map can be calculated from the ensemble by computing the ratio of mean of the signal and standard deviation of the noise-only reconstructions for each pixel across the trials. Further details of the implementation of this Monte Carlo simulation are provided below. Comparison of the non-accelerated SNR_0 to the accelerated SNR_0 can provide the GRAPPA g-factor. The final expressions for SNR_0 implicitly incorporate the $\sqrt{R}$ penalty incurred by accelerated imaging by including the number of *k*-space samples acquired for each image, N_{acq}.

Including the four correction factors as well as the GRAPPA g-factor explicitly, the final SNR_0 equations become

$$SNR_0^{rS_0S} = gk\frac{b_{noise}\sqrt{2}}{\sqrt{N_{acq}}}\left(\frac{S^H S}{\sqrt{S^H \Psi S}}\right) \tag{7}$$

$$SNR_0^{cov-rS_0S} = gk\frac{b_{noise}\sqrt{2}}{\sqrt{N_{acq}}}\left(\sqrt{S^H\Psi^{-1}S}\right) \quad (8)$$

where N_{acq} represents the number of *k*-space samples acquired, $\boldsymbol{b}_{\mathbf{noise}}$ is the correction for the noise bandwidth, $\sqrt{2}$ is the correction factor for real-valued data, $\boldsymbol{k}$ accounts for changes in noise statistic distribution and *g* is the coil geometry factor. For non-accelerated scans, $g = 1$ for all pixels.

METHODS

Image acquisition used a Siemens 3T MAGNETOM Trio, A Tim System, (Siemens Healthcare, Erlangen, Germany). Data were acquired using three different RF coils: a Transmit/Receive volume birdcage head coil (USA Instruments Inc.), a Siemens 12Ch receive-only head phased array, and a prototype 32Ch receive-only phased array head coil with a similar design as the product Siemens 32Ch array. The accelerated EPI acquisitions used the product 32Ch and 12Ch phased arrays.

To achieve accurate comparison between the coils, the same four healthy volunteers were scanned using all three coils to perform the flip angle and resolution-dependence comparison. Another four healthy human subjects were imaged using the 12Ch and the 32Ch arrays to investigate the effect of acceleration in parallel imaging on the tSNR.

Written consent was obtained from all the subjects under protocols approved by institutional review board. Head immobilization was achieved using foam pads. Automatic slice prescription, based on alignment of localizer scans to a multi-subject atlas, was used to achieve a consistent head position across subjects and multiple scanning sessions with the different RF coils. Resting state EPI time-series were collected using a single-shot gradient echo EPI sequence. All subjects were asked to relax while in the scanner with their eyes closed; no specific stimulus was applied. Prior to each scan, four images were acquired and discarded to allow longitudinal magnetization to reach equilibrium. For all the above experiments, raw *k*-space data were saved for offline reconstructions and analysis. The offline data reconstruction was undertaken to ensure that all aspects of the image reconstruction (e.g., filtering) were known and under our control. Data without RF excitation were also obtained for all EPI acquisitions to determine the thermal image noise, σ_0, and noise covariance matrix, $\boldsymbol{\psi}$. Fig. 2 shows an example of non-accelerated high resolution EPI images (1×1×3 mm^3) acquired with the 32Ch array.

Data Acquisition

Non-accelerated EPI with Variable Flip Angle, Resolution for 1Ch, 12Ch and 32Ch Coils—Fully relaxed (TR=5400ms) gradient-echo EPI time-series were acquired to evaluate the signal and noise characteristics as a function of RF coil, flip angle and in-plane spatial resolution. In the first experiment, data were collected at five different nominal flip angles (12°, 24°, 37°, 53° and 90°) using TR / TE = 5400 ms / 30 ms, 60 time points, FOV = 240 × 240 mm^2, matrix = 128 × 128, ten 4 mm thick slices with inter-slice gap of 2 mm with orientation parallel to the AC-PC line. The bandwidth and echo spacing were selected to be 1562 Hz/pixel and 0.7 ms, respectively. Additional time-series at six different resolutions were acquired in the second experiment using TR / TE / flip = 5400 ms / 30 ms / 90° and fifteen 3mm thick slices with a slice gap of 3mm, and in-plane resolutions of 1×1 mm^2, 1.5×1.5 mm^2, 2×2 mm^2, 3×3 mm^2, 4×4 mm^2 and 5×5 mm^2. Other acquisition parameters, such as bandwidth, echo spacing, partial Fourier factor, etc., were chosen to optimize the

EPI acquisition at each resolution and are shown in Table 1. Phantom data were also collected with the same acquisition parameters to validate our estimates of image SNR. Because the flip angle is known to vary across the head at 3T, due to dielectric center brightening effects, all "flip angles" listed are nominal, and in our system, most accurately reflect the flip angle at the center of the head where the transmit voltage calibration measurement is performed. Actual flip angles at the edge of the head are slightly lower.

Accelerated EPI with Variable Resolution, Acceleration Factor for 12Ch and 32Ch Coils—To evaluate the effect of parallel imaging on the EPI time-series data, gradient echo resting-state EPI measurements were acquired using TR / TE / flip = 2000 ms / 30 ms / 90° and 150 time points. Data were collected with orientation parallel to the AC-PC line, at three different resolutions; 2×2×2 mm^3, 3×3×3 mm^3, 3×3×5 mm^3, using parallel imaging reconstruction (GRAPPA) with acceleration factors of 1, 2, 3 and 4 at each resolution. The acquisition parameters were again optimized for each resolution and are listed in Table 2. As above, phantom data were also collected with the same acquisition parameters to validate our estimates of image SNR.

Image Reconstruction and SNR Calculations—Image reconstruction and SNR maps computations were performed offline with custom software written in Matlab (MathWorks Inc., Natick, MA, USA). Standard EPI image reconstruction was carried out consisting of FFT operations, navigator-based phase correction to reduce Nyquist ghosting, and a gridding correction to compensate for gradient ramp sampling in the frequency encode readout. Both of these corrections were determined to have negligible effect on the final SNR_0, and no additional apodization filtering was applied to the image data at any stage of the reconstruction. In the cases using partial Fourier acquisitions, the zero-filling method was chosen to avoid unnecessary filtering of the data. The effect of zero-filling on the final SNR_0 was taken into account by normalizing the noise standard deviation by the number of acquired *k*-space samples rather than the final number of pixels in the reconstructed image as mentioned in the *Theory* section.

Images reconstructed from each individual coil element were combined either with the root sum-of-squares combination method (rSoS) (Eq. 3), or with the noise covariance weighted root sum-of-squares combination method (cov-rSoS) (Eq. 4), which incorporates the channel noise covariance matrix to improve the SNR in the final, combined image.

Accelerated data reconstructions were performed using the manufacturer's GRAPPA reconstruction algorithm. The SNR_0 maps for the accelerated images were calculated using the Monte Carlo method (Robson et al. 2008) described in the *Theory* section with Monte Carlo trails generated using an offline version of the manufacturer's GRAPPA code. For each accelerated acquisition we estimated the noise covariance matrix from a noise-only measurement collected in the absence of any RF excitation but with the identical protocol (except for the number of measurements, which was 20 rather than 150) and, in particular, a matching pixel bandwidth. After correcting for the measured effective noise bandwidth (which ranged in value from about 0.78 to 0.81), this noise covariance matrix was used to generate synthetic noise with the same statistics as the measured thermal noise. For each EPI run, we averaged the first 10 measurements of the time-series in *k*-space to reduce noise and generate a single high-SNR reference measurement to measure the image signal. We then generated 150 replicas of this reference measurement and added an independently generated sample of synthetic noise to each replica of the *k*-space data. This synthetic *k*-space data were fed through the manufacturer's image reconstruction system. SNR_0 was estimated from the resulting magnitude images by computing the ratio of the mean and standard deviation, calculated over the replicas at each pixel, and corrected for the bias in both the

mean and standard deviation (as described above, *Theory* section) to generate an unbiased estimate of SNR_0.

Data Analysis

Once the image data were reconstructed, the AFNI motion correction algorithm (Cox and Jesmanowicz 1999) was applied to remove subject related movement artifact that would cause time-course instability. Linear trends were also removed. At all experiments, tSNR maps were estimated from the motion corrected and detrended EPI time-series as the mean intensity value of an ROI or pixel across the time points divided by its temporal standard deviation, then corrected as described above to remove the magnitude bias. SNR_0 maps were generated as described in the previous section. Measurements of tSNR and SNR_0 were evaluated in cortical gray matter regions-of-interest (ROIs) at each slice. The gray matter masks were manually selected to cover cortical areas of frontal, temporal, occipital and parietal cortex over all the slices (shown in Fig. 2) and across subjects.

For the various SNR_0 modulations via flip angle, resolution, coil selection, and acceleration factor, the tSNR was examined as a function of SNR_0. The relationship of tSNR to SNR_0 was fit to the model of Eq. 1, using a non-linear least squares algorithm available in Matlab (MathWorks Inc., Natick, MA, USA). The constant λ was estimated during the fitting and the tSNR asymptote was calculated as $1/\lambda$ (Kruger and Glover 2001). The ratio of physiological noise to thermal noise was estimated from the measurements of tSNR and SNR_0 using Eq. 2.

RESULTS

Non-accelerated EPI with Variable Flip Angle, Resolution for 1Ch, 12Ch and 32Ch Coils

Fig. 3 shows representative SNR_0^{rSoS} maps derived from non-accelerated EPI data using Eq. 7, corresponding to the 1Ch coil, 12Ch and 32Ch arrays; the maps are shown with the same grayscale. Fig. 4 shows SNR_0 in cortical ROIs plotted as a function of flip angle for the three coil configurations using both SNR^{rSoS} and $SNR^{cov\text{-}rSoS}$ individual channels combinations. For each coil, SNR_0 increases as the sine of the flip angle (shown with dotted line) and also shows substantial increases in the cortex for the array coils. The cov-rSoS combination of individual channels shows increased SNR_0 in the array coil acquisitions. For example, an average of 40% increase in SNR_0 was observed on the 32Ch coil with the cov-rSoS combination compared to the rSoS. Increases in tSNR, however, were more moderate with an average of 10% obtained with the cov-rSoS versus the rSoS combination.

Fig. 5 shows tSNR as a function of SNR_0 for the non-accelerated scans acquired with each receive coil at different flip angles and a fixed resolution of $1.9\times1.9\times4$ mm^3. Both SNR^{rSoS} and $SNR^{cov\text{-}rSoS}$ reconstructions are shown at the top and bottom panel, respectively. Each point represents the average and error-bars represent the standard deviation across all of the subjects. Blue, red and green represent data acquired with the 1Ch (Birdcage coil), 12Ch, and 32Ch arrays, respectively. Each flip angle is described by different symbol as shown in the figure legend. At higher flip angles and higher count of channels, physiological noise dominated the time-series EPI. For the rSoS combination method, a fit of this data to Eq. 1 yields an estimate of the constant λ=0.0095 with lower and upper 95% confidence limits of 0.0090 and 0.0099, respectively. Similarly, the fit of Eq. 1 to the cov-rSoS data yielded λ=0.0096 with lower and upper 95% confidence limits of 0.0092 and 0.0101, respectively. The asymptotic tSNR value ($1/\lambda$) was 105.40 and 104.40 for rSoS and cov-rSoS respectively. The dotted blue line in Fig. 5 is the line of identity ($tSNR=SNR_0$).

Fig. 6 illustrates the dependence of tSNR on SNR_0 for the non-accelerated scans when SNR_0 was modulated by coil choice and voxel volume. Again, blue, red and green indicate

1Ch (Birdcage coil), 12Ch, and 32Ch coils, respectively. The various symbols correspond to the different voxel sizes used. Our results show that at lower resolutions, as SNR_0 increases, the same asymptotic behavior was observed for the tSNR as previously reported (Triantafyllou et al. 2005). However, at the high spatial resolution acquisitions, the larger array coils provided increases in tSNR. For example, for the rSoS combination method, the 32Ch coil increased the tSNR of the 1.5×1.5×3 mm^3 acquisition by 48% compared to 12Ch coil. At lower resolutions however, (e.g. 5×5×3 mm^3) the increase was only 11%. Fitting of all the data to the noise model (Eq. 1) gave: λ=0.0080 with lower and upper 95% confidence limits of 0.0075 and 0.0085 respectively, giving an asymptotic tSNR of 125.0. For each coil configuration, fitting the data to Eq. 1 gave λ_{1Ch}=0.0079 (0.0074, 0.0083), λ_{12Ch} = 0.0080 (0.0072, 0.0093), λ_{32Ch} = 0.0081 (0.0068, 0.0092), with numbers in parenthesis corresponding to lower and upper 95% confidence limits. The above values of λ correspond to the asymptotic limit for tSNR ($1/\lambda$) of 126.6, 125.0 and 123.5 for 1Ch, 12Ch, and 32Ch coils, respectively, for rSoS coil elements combination. Similarly, when the cov-rSoS combination method was used (Fig. 6 lower panel), fitting of all the data to the noise model (Eq. 1) yielded λ=0.0081 with lower and upper 95% confidence limits of 0.0075 and 0.0085 respectively, resulting in an asymptotic tSNR of ~124.0.

The ratio of physiological to thermal noise (σ_p/σ_0) calculated from Eq. 2 for the non-accelerated scans at each coil, flip-angle and resolution are given in Tables 3 and 4, respectively. The 1Ch acquisitions produced thermal noise dominated images for all flip angles and resolutions. The 12Ch coil was thermal noise dominated for all flip angles under rSoS reconstructions and became physiological noise dominated for higher flip angles under the cov-rSoS coil elements combination. Apart from the flip angle = 12°, the 32Ch array data was physiological noise dominated for all flip angles and both image combination methods. For example, at flip angle of 90°, the σ_p/σ_0 ratio increased from 0.91 to 2.99 from the 12Ch to 32Ch for images combined with the rSoS, and resulted in even higher ratios 1.72 and 4.19 for 12Ch and 32Ch, respectively, when the cov-rSoS used. Thermal noise dominated images were observed at high resolutions with the 12Ch coil for rSoS combination. The 32Ch array data was physiological noise dominated for all spatial resolutions studied here and both coil elements combinations. The physiological to thermal noise ratio, for example, increased from 0.90 to 2.87 for the 12Ch to 32Ch array for rSoS combination. The cross-over point between thermal noise dominance and physiological noise dominance is defined as the voxel volume for which $\sigma_0=\sigma_p$. This was determined from a linear interpolation of the data in Table 4 to occur at voxel volumes of 86.50 mm^3, 16.92 mm^3, 0.84 mm^3 for the single channel, 12Ch and 32Ch coil where the array channels were combined with the rSoS method and 4.81 mm^3, for the 12Ch coil using cov-rSOS combination. For the 32Ch using the cov-rSoS combination, the σ_p/σ_0 ratio does not reach unity with linear extrapolation of our data. The single channel result is identical under these two analyses since no combination of channels is required.

Accelerated EPI with Variable Resolution, Acceleration Factor for 12Ch and 32Ch coils

Fig. 7 shows measurements of tSNR as a function of SNR_0 for accelerated EPI acquisitions at different in-plane spatial resolutions and coil configurations. Red and green symbols correspond to the 12Ch and 32Ch coils, respectively, whereas squares, circles and diamonds represent resolutions of 2×2×2 mm^3, 3×3×3 mm^3, 3×3×5 mm^3, respectively, for each coil. At each resolution data was acquired with acceleration factor of R=1, 2, 3 or 4 (with R=1 indicating non-accelerated acquisitions). Our findings show that accelerated data can also be parameterized with the same model as the non-accelerated images (Kruger and Glover 2001,Triantafyllou et al. 2005); As SNR_0 increases, tSNR approaches its asymptote for lower resolutions and lower acceleration factors. At higher acceleration factors (e.g. R=4) and higher resolutions we are at the thermal noise dominated regime of the noise model (Eq.

1). Fitting all the data (both coil arrays, all resolutions and all acceleration factors) to the noise model gave λ=0.0089 with lower and upper 95% confidence limits of 0.0083 and 0.0095 respectively, giving an asymptotic tSNR of ~115.0, similar to that of non-accelerated scans.

Fig. 8 shows the tSNR (top row) and the SNR_0 (bottom row) as a function of resolution at acceleration rates of *R*=1, 2, 3, and 4, for 12Ch and 32Ch coils. Each bar represents the average and error-bars represent the standard deviation across all of the subjects. Time-series SNR decreases at higher resolutions as expected but it is also reduced with higher *R* in all cases. For example for the 32Ch coil, at the lowest resolution 3×3×5 mm^3 tSNR reduced by ~40% between the non-accelerated acquisition and the *R*=4 acquisition, and at higher resolution of 2×2×2 mm^3 the reduction was ~45%. Similarly, image SNR decreases at higher resolutions, however the degradation across acceleration rates is faster than tSNR. When the 32Ch coil used, SNR_0 showed a 69% decrease between the non-accelerated and the R=4 accelerated acquisitions at voxel size of 3×3×5 mm^3, an approximate 20% more decrease compared to the tSNR at the same resolution.

Fig. 9 shows the relationship of tSNR and SNR_0 from phantom data for different accelerations, in-plane spatial resolutions and coil configurations. Squares and circles correspond to accelerations and resolutions, respectively; red corresponds to data acquired with the 12Ch coil and green to the 32Ch phased array. Each point represents the average and error-bars represent the standard deviation calculated from ROIs in the phantom. The solid line represents again the line of identity (tSNR=SNR_0) and the dotted line corresponds to the human data from Fig. 6. Individual coil elements were combined with the SNR^{rSoS} method. For all experiments the phantom data show higher SNR estimates compared to the human data, for both SNR_0 and tSNR and the phantom data is considerably closer to the line of identity than the human data. Deviations from the line of identity for the phantom experiments are likely due to system instabilities captured in EPI time-series data. At lower resolution (higher SNR_0) the deviation from the line of identity is larger particularly for the 32Ch array coil, suggesting that these instabilities are higher for larger signal intensities.

DISCUSSION

In this paper we examined the fMRI time-series fluctuations compared to thermal noise, when parallel imaging and multiple array coils are used. In particular, we investigated the relationship between tSNR and SNR_0 as a function of acquisition parameters such as flip angle, in-plane image resolution, degree of acceleration, and receive coil used. We took care to measure SNR_0 and tSNR maps in a rigorous way that allowed their direct comparison of these SNR metrics and thus allow the determination of the ratio of physiological to thermal noise for each acquisition. In order to assess the effect of omitting the correction factors, which described by Kellman and McVeigh (Kellman and McVeigh 2005, Kellman and McVeigh 2007), on the image and time-series SNR maps, we have recalculated the SNR values without these corrections and present the new graphs and additional discussion in the Supplementary Material (Figure S1).

Our findings demonstrate that when SNR_0 is modulated by flip angle, image resolution and coil performance, the physiological noise is well modeled as proportional to the signal. As a result, the tSNR approaches an asymptote at higher flip angles, lower resolutions and highly parallel array coils. Our results suggest that the relationship between tSNR and SNR_0 can be well parameterized by the Kruger and Glover model for all different acquisition parameters, accelerations, and coil configurations. At low values of SNR_0 (small voxels or lower coil performance), the tSNR is dominated by thermal image noise and grows linearly with SNR_0. As the image SNR increases (above approximately 200), the curve approaches an asymptote

and additional improvement in SNR_0 does not translate to substantial gains in tSNR. Since the highly parallel array coils mainly increase image SNR, this suggests that their biggest benefits for fMRI (for which tSNR is the figure of merit) will be for higher image resolutions where SNR_0 is below 200. The asymptotic tSNR (1/λ) showed a slight variation across the different experiments. One factor that might contribute to this is that the voxel volumes used have different levels of partial volume with white matter and CSF. For example, the maximum voxel volume used in the flip angle experiment was 16 mm^3, in the accelerated imaging experiments was 45 mm^3, while the resolution data contained voxel volumes up to 75 mm^3. If partial volume was the significant bias, then the fact that this study showed the highest asymptotic tSNR (1/λ) suggests that partial voluming with white matter might have been more significant.

Because tSNR is defined by the signal variance across time, the precision of the tSNR estimation is affected by the accuracy of the noise SD estimation, which is a function of the number of time-points (N_{tp}) acquired for each experiment. The error in estimating variance in a finite duration time-series diminishes as the N_{tp} increases. A Monte Carlo determination of the RMS error expected in the standard deviation calculated for our accelerated experiments (N_{tp}=150) shows an expected zero-mean RMS error of 5.8%. For the non-accelerated experiments (N_{tp}=60) the expected RMS error is about 9.2%. An assessment of this uncertainty as a function of N_{tp} is given also in the Supplementary Material, Figure S2.

At high field strengths, (≥3T), there is an inherited flip angle variation across the head, due to RF field (B_1^+) inhomogeneity in the excitation process. In our system the nominal flip angle correctly describes the excitation in the center of the head, but the periphery and especially inferior temporal cortex experiences lower flip-angles. Because the cortical ROI is peripheral, the cortical SNR_0 of the acquired scans is likely lower than would be expected if the flip angle was set specifically for this region. However, for the 90° excitations used, the effect on signal levels is small; for example, a 15% center brightening effect would translate to a 2% decrease in SNR_0.

Two different methods for coil element combination were examined; the root sum-of-squares combination method (rSoS) and the noise covariance weighted root sum-of-squares combination method (cov-rSoS), which incorporates the channel noise covariance matrix to improve the SNR in the final, combined image. For each coil, SNR_0 increases as the sine of the flip angle and also shows substantial increases in the cortex for the array coils. The cov-rSoS combination of individual channels shows increased SNR_0 in the array coil acquisitions. The image SNR improvement from the more sophisticated method, however simply moved the SNR points along the asymptotic line described by the Kruger and Glover model, resulting in modest gains in tSNR for physiological noise dominated acquisitions but larger gains for thermal noise dominated acquisitions (for the data in Fig. 5, this corresponded to the lower flip angles). The ratio of physiological to thermal noise (σ_p/σ_0) also increased when the cov-rSoS combination method is used (see Tables 3 and 4) compared to when the rSoS method is used. Since the signal level is not expected to change between the two combination methods, the σ_p/σ_0 increases suggest that σ_0 is reduced by the cov-rSoS method, a conclusion supported by the improved SNR_0 in the cov-rSoS method shown in Fig. 4. Furthermore the assumed noise model (Kruger and Glover 2001) would predict that σ_p would remain unchanged with the two combination methods, since physiological noise is modeled as scaling with the amplitude of the MR signal (S), with proportionality constant λ, or $\sigma_p=\lambda S$, and S remains unchanged.

Other studies have reported the measurements of physiological fluctuations in functional MRI. Those studies could directly compare tSNR and SNR_0 and determine the physiological to thermal noise ratio of each acquisition, but only addressed the simplified situation of

single-channel reception (Kruger and Glover 2001, Triantafyllou et al. 2005, Yacoub et al. 2005, Triantafyllou et al. 2006) and therefore non-accelerated imaging. Alternatively, de Zwart et al. (de Zwart et al. 2002) studied the effects of physiological noise in parallel imaging acquisitions, including the effects of acceleration. The study of de Zwart et al. reports signal-normalized noise measurements (noise standard deviation as a percentage of the signal level), such as, σ_i^{full}, which, in their notation, represents the signal-normalized noise level for the intrinsic (thermal) noise with an non-accelerated (R=1) (full) acquisition, and σ_t^{full}, which represents the corresponding measure for the time-series fluctuations; (In our notation, $\sigma_i^{full}=\frac{1}{SNR_0}$ and $\sigma_t^{full}=\frac{1}{tSNR}$ for non-accelerated acquisition). Similarly, the measure σ_i^{SENSE} and σ_t^{SENSE} in the study of de Zwart et al. refers to the signal-normalized thermal and temporal noise levels for an R=2 SENSE acquisition. They compare non-accelerated tSNR to the accelerated tSNR in a model that assumes that the SENSE g-factor and reduction factor R affect only the image noise, and demonstrate that their data supports this model. A similar assumption is inherent in our model through our formulation of image SNR for accelerated scans (Eq. 7, 8), and our measurements support the conclusion that while the noise penalties of accelerated imaging accrue and reduce image SNR, they have less impact on tSNR in the physiological noise dominated regime. This degradation in tSNR, however, is small, relative to the decreases introduced by the acceleration on image SNR, and not in small in absolute units. In this case, functional imaging can generally withstand substantially more acceleration than conventional anatomical imaging; a conclusion supporting deZwart's conclusion. Our work additionally verifies this important conclusion for current array configurations and field strengths (up to 32Ch arrays as opposed to 4Ch, and 3T instead of 1.5T), as well as higher acceleration factors (up to R=4 as opposed to R=2). Additionally we extend the study to multiple resolutions. We expect that given these technological advances in coil and high-field technology, conventional resolution fMRI studies are substantially more physiological noise dominated than this previous work. Finally we utilize the full correction factors to generate SNR units needed for comparing image and time-series SNR values, a methodology that was fully worked out after the study of de Zwart et al. This allows us to generate physiological to thermal noise ratios for the measurements which can serve to guide the design of fMRI acquisitions.

Our measurements of tSNR and SNR_0 reveal that the same physiological noise model can be used to parameterize physiological fluctuations in accelerated EPI time-series as the one used for non-accelerated EPI when the image SNR is modulated by coil design, flip angle, resolution, or coil combination method. The increased image SNR offered by the parallel arrays, produces the greatest benefit in the tSNR for medium to small voxel volumes, and for higher acceleration factors, where the thermal noise still contributes significantly to the time-series SD (i.e. the linear segment of the curve). Therefore, parallel array coils, through their increase in image SNR, can offer an improvement in time-series SNR, in addition to the reduced echo train and decreased susceptibility distortions in EPI. Although increasing the degree of acceleration reduces tSNR, this effect is smaller than the decrease in image SNR. Furthermore, the higher acceleration rates provide less physiological noise dominated accelerated fMRI time-series compared to their non-accelerated counterparts.

CONCLUSION

Highly parallel detection of functional imaging time-series provides the potential for higher image Signal-to-Noise ratio (SNR_0) as well as decreased susceptibility distortions in echo-planar imaging. In this study we investigated the relationship of tSNR and SNR_0 when signal is modulated by coil count, flip angle, voxel volume, and degree of acceleration in parallel imaging. Special attention was given to SNR_0 calculation from the phased array images so that is comparable to tSNR. Our findings demonstrate that tSNR reaches a plateau

when SNR_0 increases with larger coil count, bigger voxel volume, and lower acceleration factor and therefore the physiological noise is well modeled as proportional to the signal for accelerated images and multi-channel phased arrays. Our study suggests that the increased image SNR offered by multi-channel arrays (e.g. 32Ch) produces the greatest benefit in the temporal SNR for medium to small voxel volumes and higher accelerations in parallel imaging, where thermal noise still contributes significantly to the fMRI time-series variance.

Research Highlights

1. Phased array coils improve image SNR in fMRI.
2. Physiological noise limits time-course SNR when multichannel arrays are used.
3. Physiological noise is proportional to the signal for accelerated MR imaging.
4. Thermal Noise dominates parallell fMR imaging with high acceleration.

Supplementary Material

Refer to Web version on PubMed Central for supplementary material.

Acknowledgments

The authors would like to thank the McGovern Institute for Brain Research at MIT for funding, Steve Shannon and Sheeba Arnold for technical support, and Michael Hamm and Thomas Witzel for assistance with computational resources. This work was supported by NIH grant P41RR14075.

REFERENCES

Breuer FA, Kannengiesser SA, Blaimer M, Seiberlich N, Jakob PM, Griswold MA. General formulation for quantitative G-factor calculation in GRAPPA reconstructions. Magn Reson Med. 2009

Constantinides CD, Atalar E, McVeigh ER. Signal-to-noise measurements in magnitude images from NMR phased arrays. Magn Reson Med 1997;38:852–7. [PubMed: 9358462]

Cox RW, Jesmanowicz A. Real-time 3D image registration for functional MRI. Magn Reson Med 1999;42:1014–8. [PubMed: 10571921]

de Zwart JA, van Gelderen P, Kellman P, Duyn JH. Application of sensitivity-encoded echo-planar imaging for blood oxygen level-dependent functional brain imaging. Magn Reson Med 2002;48:1011–20. [PubMed: 12465111]

Griswold MA, Jakob PM, Heidemann RM, Nittka M, Jellus V, Wang J, Kiefer B, Haase A. Generalized autocalibrating partially parallel acquisitions (GRAPPA). Magn Reson Med 2002;47:1202–10. [PubMed: 12111967]

Gudbjartsson H, Patz S. The Rician distribution of noisy MRI data. Magn Reson Med 1995;34:910–4. [PubMed: 8598820]

Henkelman RM. Measurement of signal intensities in the presence of noise in MR images. Med Phys 1985;12:232–3. [PubMed: 4000083]

Kellman P, McVeigh ER. Image reconstruction in SNR units: a general method for SNR measurement. Magn Reson Med 2005;54:1439–47. [PubMed: 16261576]

Kellman P, McVeigh ER. Magn Reson Med 2007;58:2. Erratum.

Kruger G, Glover GH. Physiological noise in oxygenation-sensitive magnetic resonance imaging. Magn Reson Med 2001;46:631–7. [PubMed: 11590638]

Pruessmann KP, Weiger M, Scheidegger MB, Boesiger P. SENSE: sensitivity encoding for fast MRI. Magn Reson Med 1999;42:952–62. [PubMed: 10542355]

Robson PM, Grant AK, Madhuranthakam AJ, Lattanzi R, Sodickson DK, McKenzie CA. Comprehensive quantification of signal-to-noise ratio and g-factor for image-based and k-space-based parallel imaging reconstructions. Magn Reson Med 2008;60:895–907. [PubMed: 18816810]

Roemer PB, Edelstein WA, Hayes CE, Souza SP, Mueller OM. The NMR phased array. Magn Reson Med 1990;16:192–225. [PubMed: 2266841]

Triantafyllou C, Hoge RD, Krueger G, Wiggins CJ, Potthast A, Wiggins GC, Wald LL. Comparison of physiological noise at 1.5 T, 3 T and 7 T and optimization of fMRI acquisition parameters. Neuroimage 2005;26:243–50. [PubMed: 15862224]

Triantafyllou C, Hoge RD, Wald LL. Effect of spatial smoothing on physiological noise in high-resolution fMRI. Neuroimage 2006;32:551–7. [PubMed: 16815038]

Triantafyllou, C.; Polimeni, JR.; Wald, LL. Physiological Noise in Gradient Echo and Spin Echo EPI using Multi-Channel Array Coils; Proceedings 16th Annual Scientific Meeting, International Society for Magnetic Resonance in Medicine; 2008; p. 2465

Wright SM, Wald LL. Theory and application of array coils in MR spectroscopy. NMR Biomed 1997;10:394–410. [PubMed: 9542737]

Yacoub E, Van De Moortele PF, Shmuel A, Ugurbil K. Signal and noise characteristics of Hahn SE and GE BOLD fMRI at 7 T in humans. Neuroimage 2005;24:738–50. [PubMed: 15652309]

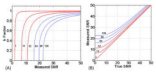

Figure 1.

Magnitude detection biases the SNR calculation increasingly with larger coil arrays and increasingly at lower measured SNR. (A) The correction factor ***k*** needed to determine the true SNR for a magnitude image given an SNR measured under the assumption of Gaussian-distributed noise. For a single-channel coil and in regions without signal, the measured noise SD must be scaled by 0.65 as given by Gudbjartsson and Patz (Gudbjartsson and Patz 1995). The plot in panel (A) provides the generalization of this constant as a function of measured SNR for array coils of 1, 12, 32, 64, 96 and 128 elements, extending the plots of Constantinides et al. (Constantinides et al. 1997) to the large array case. (B) The same information depicted as the relationship between the measured SNR (assuming Gaussian statistics) and the true SNR for the different array channel counts. The red traces correspond to the channel counts of the arrays used in this study (1, 12, and 32).

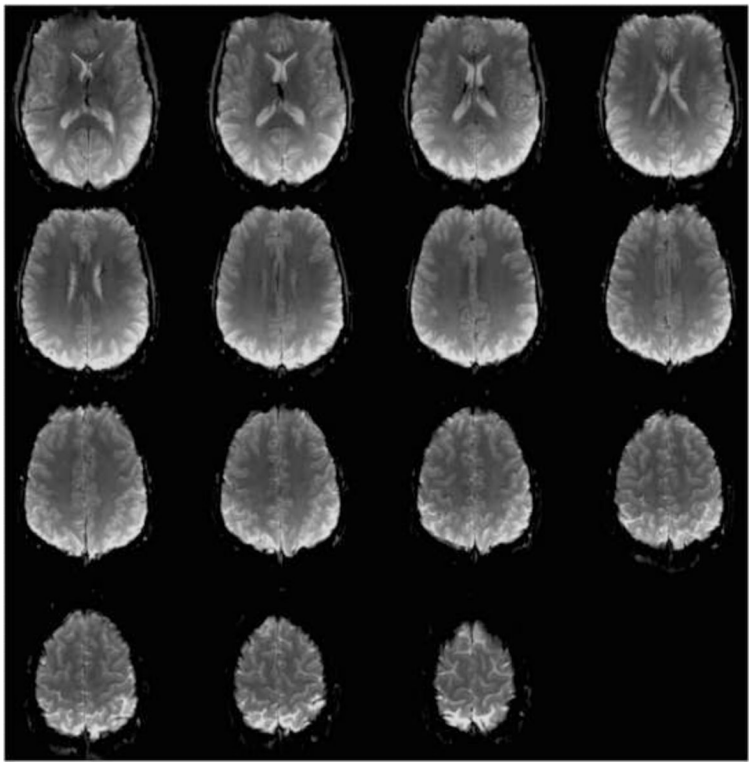

Figure 2.
Non-accelerated high resolution ($1\times1\times3mm^3$) EPI images acquired with the 32Ch array.

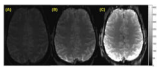

Figure 3.

Image SNR maps (in SNR units) generated using SNR^{rSoS} method for 1Ch (birdcage), 12Ch and 32Ch coils respectively derived from non-accelerated EPI time-course, with voxel size of $1.5\times1.5\times3mm^3$. All images are at the same grayscale level.

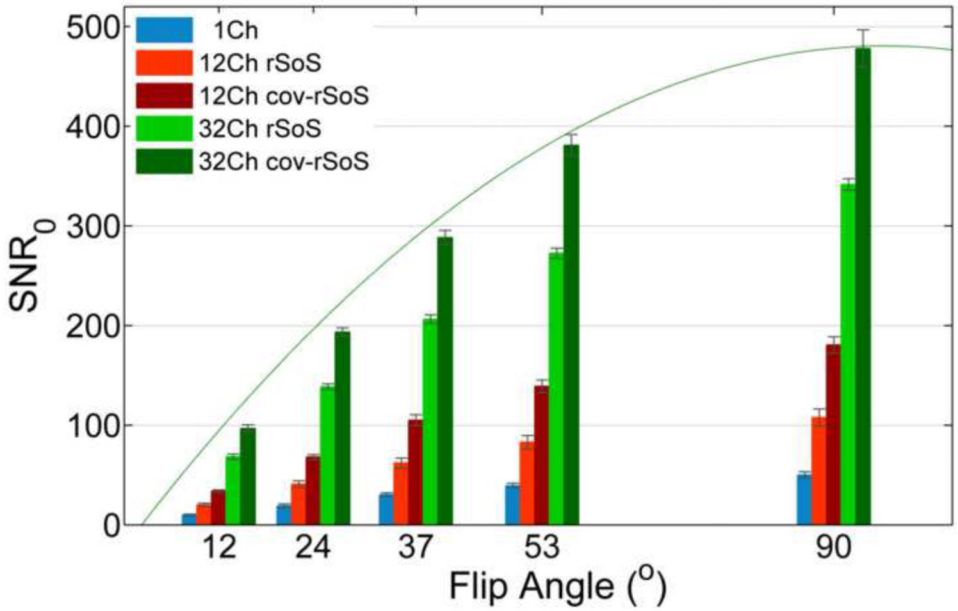

Figure 4.

Image SNR (SNR_0) as a function of flip angle for each coil, using both SNR_0^{rSoS} and $SNR_0^{cov\text{-}rSoS}$ coils elements combinations. Measurements derived from areas of cortical gray matter ROIs and are averages over four subjects.

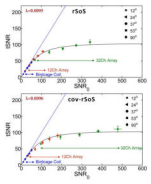

Figure 5.

SNR in fMRI time-series (tSNR) as a function of image SNR (SNR_0) for different flip angles, at a constant resolution of 1.9×1.9×4 mm^3, for the Birdcage coil (blue), 12Ch array coil (red) and 32Ch array (green). Both SNR_0^{rSoS} and $SNR^{cov\text{-}rSoS}$ are shown on top and lower panels, respectively. Each point represents the average and SD error bars in areas of cortical gray matter over all four subjects, (because of their small size, some of the error bars are contained within the symbols). The dotted blue line represents the line of identity ($tSNR=SNR_0$) and the solid gray line corresponds to the fit of Eq. 1 to all data.

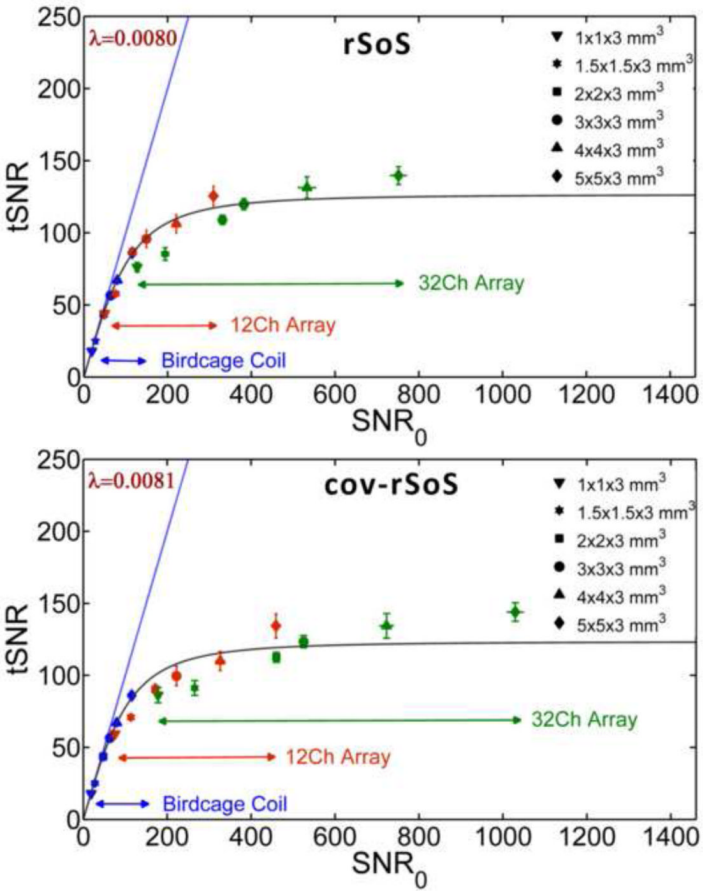

Figure 6.

Time-series SNR as a function of image SNR (SNR_0) for the Birdcage coil (blue), 12Ch array coil (red) and 32Ch array (green). On the top, data were generated by combining the individual coil elements with the root sum-of-squares combination method (rSoS), while on the lower panel the noise covariance weighted root sum-of-squares (cov-rSoS) combination was used. SNR_0 was modulated by varying the voxel size. Figure legends show the various resolutions used and the corresponding symbols. Each point on the graph represents the average and SD in areas of cortical gray matter over all four subjects for each coil; (because of their small size, some of the SD error-bars are contained within the symbols). The dotted blue line is the line of identity ($tSNR=SNR_0$), and the solid line corresponds to the model fit of Eq. 1.

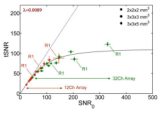

Figure 7.

Time-series SNR as a function of SNR_0 for accelerated time-series, at different spatial resolutions, and channel count (12Ch in red and 32Ch in green) for accelerations of R=1, 2, 3, and 4. Blue dotted line is the line of identity ($tSNR=SNR_0$) and solid gray line is the fit to the noise model (Eq. 1). Squares, circles and diamonds correspond to resolutions of 2×2×2 mm^3, 3×3×3 mm^3, and 3×3×5 mm^3, respectively. Data are averaged values from all four subjects derived from ROIs of cortical gray matter. Labels 'R1' indicate the non-accelerated data points for each of the resolutions. Data points corresponding to accelerated images of R=2, 3, and 4 are extended to the left of the non-accelerated data points at each resolution.

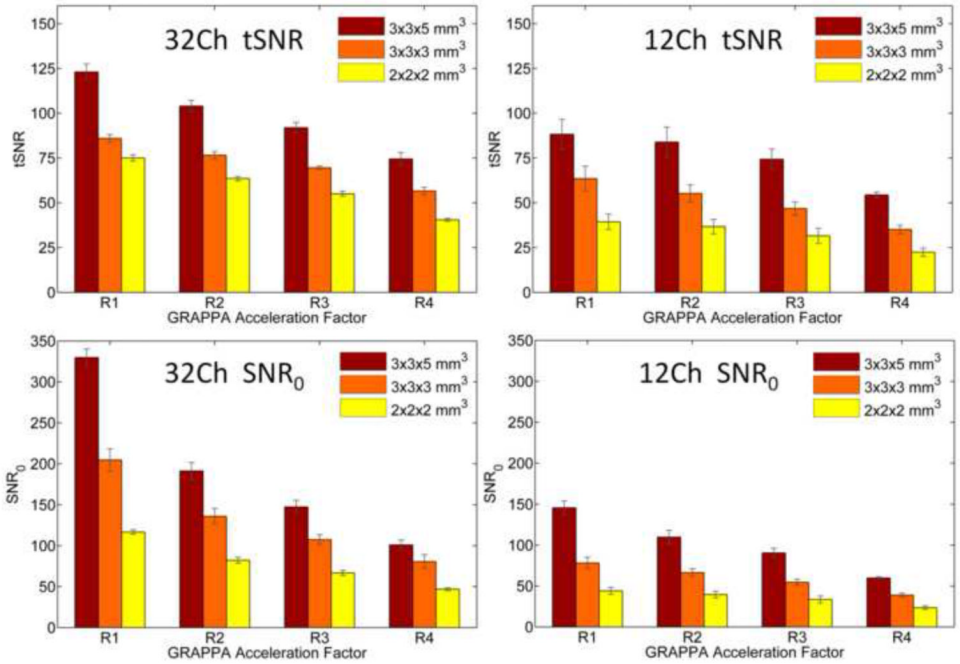

Figure 8.

SNR as a function of GRAPPA acceleration factor for EPI time-series, at different spatial resolutions, and coil configurations. Top row shows the time-course SNR (tSNR) and bottom illustrates image SNR (SNR_0). Each bar represents the average from multiple gray matter ROIs and error-bars represent the standard deviation across all of the subjects. Labels 'R1' indicate the non-accelerated data points for each of the resolutions.

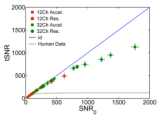

Figure 9.

Time-series SNR as a function of SNR_0 for phantom data at different spatial resolutions, accelerations and channel count (12Ch and 32Ch). Solid line is the line of identity ($tSNR=SNR_0$) and the dotted line corresponds to human data given in Figure 6. Red and green symbols correspond to 12Ch and 32Ch, respectively.

Table 1

Acquisition parameters for the resting-state EPI time-series at various resolutions

Resolution (mm^3)	FOV (mm^2)	Matrix	TE (ms)	Partial Fourier	BW (Hz/px)	Echo Spacing (ms)
1×1×3	192×192	192×192	32	5/8	1042	1.03
1.5×1.5×3	192×192	128×128	30	6/8	1502	0.75
2×2×3	256×256	128×128	30	6/8	1562	0.70
3×3×3	192×192	64×64	30	8/8	2298	0.50
4×4×3	256×256	64×64	30	8/8	3256	0.41
5×5×3	320×320	64×64	30	8/8	3720	0.36

Table 2

Acquisition parameters for the resting-state accelerated EPI time-series at various resolutions

Resolution (mm^3)	FOV (mm^2)	Matrix	TE (ms)	Partial Fourier	BW (Hz/px)	Echo Spacing (ms)
2×2×2	192×192	96×96	30	6/8	1578	0.70
3×3×3	192×192	64×64	30	8/8	2298	0.50
3×3×5	192×192	64×64	30	8/8	2298	0.50

Table 3

Ratio of σ_p / σ_0 calculated from the SNR_0 and tSNR measurements for each coil and flip-angle (FA) at a fixed spatial resolution of $1.9 \times 1.9 \times 4$ mm^3

FA (°)	1Ch	12Ch rSoS	12Ch cov-rSoS	32Ch rSoS	32Ch cov-rSoS
12	0.27±0.21	0.31±0.05	0.58±0.14	0.83±0.11	1.10±0.09
24	0.33±0.29	0.39±0.28	0.97±0.19	1.50±0.15	1.99±0.21
37	0.36±0.25	0.50±0.23	1.15±0.19	2.11±0.16	2.91±0.19
53	0.46±0.20	0.77±0.20	1.42±0.22	2.59±0.10	3.51±0.18
90	0.51±0.27	0.91±0.19	1.72±0.19	2.99±0.24	4.19±0.40

Table 4

Ratio of σ_p / σ_0 calculated from the SNR_0 and tSNR measurements for each coil and spatial resolution

Resolution (mm^3)	1Ch	12Ch rSoS	12Ch cov-rSoS	32Ch rSoS	32Ch cov-rSoS
1×1×3	0.28±0.21	0.52±0.05	0.79±0.10	1.34±0.12	1.80±0.15
1.5×1.5×3	0.42±0.35	0.86±0.07	1.25±0.11	2.04±0.17	2.73±0.18
2×2×3	0.46±0.33	0.90±0.10	1.62±0.12	2.87±0.14	3.96±0.13
3×3×3	0.51±0.10	1.20±0.08	1.99±0.18	3.03±0.13	4.13±0.15
4×4×3	0.65±0.15	1.91±0.13	2.79±0.21	3.93±0.29	5.28±0.40
5×5×3	0.89±0.16	2.26±0.15	3.27±0.26	5.28±0.28	7.08±0.38